



CHORUS

This is the accepted manuscript made available via CHORUS. The article has been published as:

Aggregation of poly(p-phenylene terephthalamide) chains: Emergence of fiber defects

Santosh Mogurampelly, Christopher M. MacDermaid, Simona Percec, Michael L. Klein, and
Giacomo Fiorin

Phys. Rev. Materials **3**, 015602 — Published 30 January 2019

DOI: [10.1103/PhysRevMaterials.3.015602](https://doi.org/10.1103/PhysRevMaterials.3.015602)

Aggregation of poly(*p*-phenylene terephthalamide) chains: emergence of fiber defects

Santosh Mogurampelly, Christopher M. MacDermaid,

Simona Percec, Michael L. Klein, and Giacomo Fiorin

Institute for Computational Molecular Science (ICMS) and Temple Materials Institute (TMI),

1925 North 12th St, Philadelphia, PA 19122, USA.

Some of the strongest polymer-based fibers are obtained by processing a nematic solution of poly-*p*-phenylene terephthalamide (PPTA) in concentrated acid. Molecular dynamics simulations reveal that the lateral density of PPTA chains in the acid solution is inhomogeneous on scales shorter than the persistence length. Hairpin turns, insertions and other defects are stabilized by chain-chain contacts. These results suggest a mechanism of fiber assembly through coalescence of nano-fibrils, and an explanation for the limited strength of PPTA fibers even at high crystallinity.

I. INTRODUCTION

Fibers of poly-*p*-phenylene terephthalamide (PPTA) chains are the basis for widely used high-performance materials such as Kevlar[®] or Twaron[®]^{1,2}. Typical PPTA chains used in these materials have about 200 repeat units, corresponding to a $\sim 48,000$ Da weight or a $\sim 2,600$ Å length when fully extended. PPTA chains are predominantly aligned along the fiber’s axis, with a high degree of solid-crystalline order³. In the X-ray diffraction structures of PPTA crystals⁴, adjacent chains appear to be held together by van der Waals forces between the phenyl groups (arranged in a “herringbone” packing) and hydrogen bonds between amide groups⁵. In this structure, slippage of individual PPTA chains is limited by steric clashes, and PPTA fibers are found to sustain very high tensile and shear loads⁶⁻⁹.

PPTA chains cannot be melted, and can only be dissolved in strong acids, such as H₂SO₄. A transition from an isotropic mixture to a nematic liquid-crystal is observed above critical PPTA concentrations of the order of 8-10 wt%¹⁰⁻¹². Solid PPTA fibers are obtained by extruding the liquid-crystalline solution through a spinneret, and washing off the remaining sulfuric acid. This procedure yields fibers with a high crystallinity¹³, which can be increased further through heat and applied tension¹⁴. However, point defects and amorphous regions are likely to remain, and are the most probable cause of the weakness of PPTA-based materials^{7,14}.

Understanding the nature and impact of structural defects in PPTA is critical to obtaining PPTA-based fibers with maximal strength. Little is known, however, about the microstructure of the nematic phase of PPTA-H₂SO₄ solutions. It has been suggested that the mutual chain-chain alignment is strongest within localized “blobs” of dimensions comparable to the persistence length L_p ¹¹. Precise measurements of the variations in PPTA density at or below this scale ($L_p \sim 290$ Å¹⁵) are currently challenging.

Here, we used molecular dynamics (MD) computer simulations to investigate the structure of PPTA chains in a concentrated H₂SO₄ solution. Starting from randomized initial conditions, we observed the aggregation of short PPTA chains (up to $n = 18$ repeat units) into liquid-crystalline fibrils over a time scale of microseconds. The degree of nematic order and the effective strength of interaction between chains increase with the polymer chain length, consistently with previous measurements.

Despite the strong orientational order, the structure of most systems does not convert into a solid-crystalline form, due lack of order in the planes orthogonal to the polymer chain axis. How-

ever, we observe the formation of point defects such as wide-angle turns, loops, and insertions of H_2SO_4 molecules within a high-density PPTA region. We find that these defects, although not detectable by elastic measurements, have a major adverse effect on the ultimate strength of PPTA crystals.

II. METHODS

We used for all simulations a coarse-grained (CG) force field for PPTA, deriving empirical parameters from physical properties of small-molecule liquids (density, surface tension, partition coefficients) with the procedure of Shinoda et al.¹⁶. Intermolecular potentials previously obtained for phenyl molecules¹⁷ were employed, as well as newly derived ones for H_2SO_4 (see also Supplemental Material¹⁸). New potential parameters for the amide group ($-\text{NH}-\text{C}=\text{O}-$) were also derived: their use beyond PPTA will be discussed in separate publications.

All interactions between CG particles of the same type, as well as those between the two CG particles of the amide group, were set from experimental properties. Intermolecular potentials between CG particles of different chemical groups (benzyl, amide, and H_2SO_4) were set using the geometric combination rule of the Lennard-Jones (LJ) potential. To account for the possibility that the interaction strength between H_2SO_4 and the PPTA carbonyls is affected by proton transfer, we ran simulations at different values of the LJ-potential depth between the corresponding CG particle types. The relevant properties here discussed vary slowly over a broad range around the combination rule (Fig. S11), indicating that the results shown are stable with respect to force field parameters¹⁸. Additional refinement of an intermolecular potential between PPTA and H_2SO_4 would likely require long-time simulations with a quantum-mechanical MD protocol. The chemical structure and the corresponding CG-particle topology of one PPTA repeat unit (12 CG particles) are shown in Fig. 1.

Table I lists the simulated mixtures of H_2SO_4 and PPTA_n , where $n = 3, 6, 12,$ and 18 is the number of repeat units. For each chain length we simulated two concentrations (2 wt% and 20 wt%) of PPTA_n : the two values straddle the range of PPTA concentrations in H_2SO_4 at manufacturing conditions¹¹. The number of PPTA_n chains was chosen to keep the number of PPTA CG-particles constant across simulations, at approximately 41,500. The number of H_2SO_4 CG-particles, each representing one molecule, was approximately 411,000 and 33,600 in the 2 wt% and 20 wt% simulations, respectively. Initial configurations for PPTA_3 through PPTA_{12} were prepared by placing

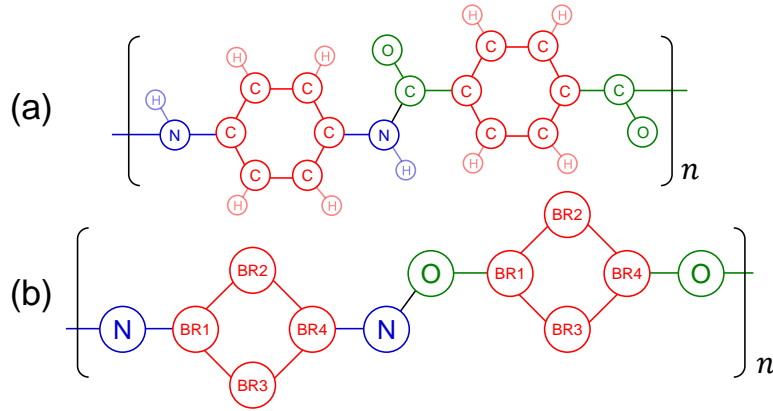


FIG. 1. **(a)** Atomic structure of PPTA (n indicates the number of repeat units). **(b)** Coarse-grained (CG) model of PPTA: “N” and “O” indicate the CG-particles of the NH and C=O amide groups, respectively.

chains at randomized positions and orientations. Additional simulations of PPTA₁₂, as well as PPTA₁₈, were prepared with randomized positions, but all orientations parallel to the z Cartesian axis (superscript “ z ”): because these simulations contain an obvious bias towards a nematic phase, they are discussed and analyzed separately. Initial configurations of each system were optimized following previously used protocols^{18,19}.

Constant-temperature, constant-pressure simulations were carried out for approximately $5 \mu\text{s}$ each, using the Nosé thermostat²⁰ and Andersen-Parrinello-Rahman barostat^{21,22} and the equations of motion of Martyna et al.²³. Equations of motion were integrated with a time step of 5 fs. The target temperature and pressure were set to the conditions immediately prior to fiber spinning (about 360 K and 1 bar)^{12,24}.

Crystals of PPTA chains were prepared from the X-ray diffraction structure of Northolt and van Aartsen⁴, by converting atomic coordinates into coordinates of the CG particles. The unit cell vectors of the crystal are $L_X = 5.2 \text{ \AA}$ (van der Waals contact direction), $L_Y = 7.9 \text{ \AA}$ (hydrogen-bond direction) and $L_Z = 12.9 \text{ \AA}$ (polymer chain direction). Energy minimization of the CG-particle positions and of the unit cell dimensions (L_X, L_Y, L_Z) was carried out, followed by constant-temperature (300 K) simulations. Models of PPTA crystals with random H₂SO₄ insertions were generated by placing H₂SO₄ molecules at random positions in the PPTA crystal, followed by energy minimization and equilibration with the same methods used for the pristine crystals.

Computations of the compressive elastic moduli E (Fig. 6) were performed by contracting or expanding one unit cell dimension by 3%, and allowing the two orthogonal dimensions to relax

2 wt% PPTA			20 wt% PPTA		
$(N \simeq 450,000)$			$(N \simeq 110,000)$		
System	N_{mol}	MW	System	N_{mol}	MW
PPTA ₃	1152	715	PPTA ₃	1728	715
PPTA ₆	576	1430	PPTA ₆	864	1430
PPTA ₁₂	288	2860	PPTA ₁₂	288	2860
PPTA ₁₂ ^z	288	2860	PPTA ₁₂ ^z	288	2860
PPTA ₁₈ ^z	192	4290	PPTA ₁₈ ^z	576	4290

TABLE I. Simulation details of PPTA_n-H₂SO₄ mixtures. N is the number of particles, N_{mol} the number of chains, and MW the molecular weight of each chain. The superscript z denotes initial conditions with chains parallel to the z -axis.

towards a target pressure of 1 bar at a temperature of 300 K. After 5 ns of equilibration, the mean of the corresponding stress tensor component was computed over 20 ns at the NVT ensemble.

Computations of shear stress-strain profiles (Fig. 7) were carried out by changing the angle between unit cell vectors in discrete steps of approximately 2° . Due to the occurrence of very large forces, the integration time step was reduced to 2.5 fs as a precaution. At each deformation, we ran 12 ns of NVT simulation, collecting the mean of the stress tensor over the last 10 ns; total simulation lengths range from 0.6 to 1 μ s.

Visualizations of supra-molecular structures shown in this paper were made with the Visual Molecular Dynamics (VMD) program²⁵.

III. RESULTS AND DISCUSSION

Local aggregation of PPTA chains. The most visible feature in all simulations of PPTA_n-H₂SO₄ mixtures chains is a tendency towards aggregation, driven by chain-chain contacts and counteracted by structural constraints generated by a combination of higher chain length (PPTA₁₂ and PPTA₁₈ systems) or high concentration (20 wt% systems). Final snapshots for $n = 12$ and 18 at 2 wt% PPTA are shown in Fig. 2; other snapshots are included in Fig. S2¹⁸. The first 10-100 ns of each simulation show aggregation of polymer chains into several small fibrils (fewer than 10 chains each; see Fig. S3)¹⁸.

At longer times, larger aggregates form by coalescence of the smaller fibrils (Fig. 2 and

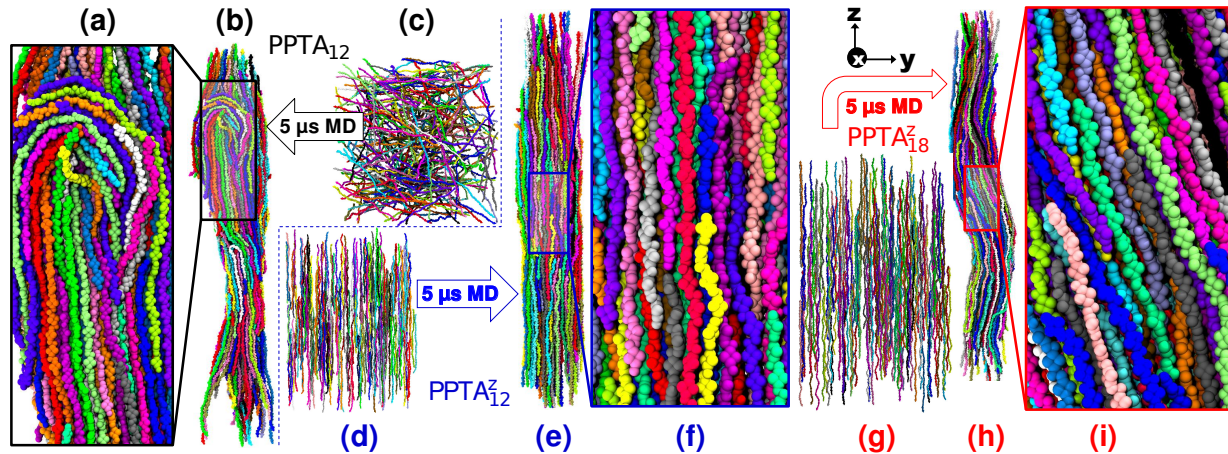


FIG. 2. Shown are the initial and final snapshots of PPTA₁₂ (a-c), PPTA₁₂^z (d-f) and PPTA₁₈^z (g-i) in liquid H₂SO₄. In all images, H₂SO₄ molecules are hidden for clarity. Snapshots for $n = 3$ and 6 are included in Fig. S2¹⁸.

Fig. S3¹⁸). During this phase, nematic order progressively increases, following a path towards energy minimization with apparent relaxation times of tens of nanoseconds (Fig. S4¹⁸). This second stage is more pronounced at 2 wt% concentration than at 20 wt%, where the movement of individual chains is impeded by a higher number of chain-chain contacts.

The probability of contacts between amide groups is found to increase with the chain length n (Fig. 3): this trend mirrors the behavior of longer PPTA chains ($n > 50$) predicted by the Maier-Saupe theory²⁶ applied to PPTA-H₂SO₄ clearing temperatures¹⁰. The density of PPTA particles along the shared director axis, $\rho(\mathbf{n} \cdot \vec{r})$, also tends to a uniform distribution over time for the higher chain lengths $n = 12$ and 18 (Fig. S7¹⁸), indicating a fairly homogeneous phase for all chains.

At both concentrations and under fully-randomized initial conditions, some of the chains assume strained conformations, such as hairpins of individual chains or bundles (see Fig. 2a-b). Given the long diffusion times (the viscosity of PPTA-H₂SO₄ is about 10^6 Pa \times sec²⁷, or 10^9 times that of liquid water) it is reasonable to assume that many such defects remain kinetically trapped in the PPTA solid fibers. In our simulations with initially parallel chains, hairpins are not observed but some chains feature wide-angle turns, particularly PPTA₁₈^z at 2 wt% (Fig. 2h) and 20 wt% (Fig. S5¹⁸).

PPTA chains achieve high nematic liquid-crystalline order. Alignment between chains was quantified by the nematic order parameter, S_2 :

$$S_2 \equiv \left\langle \frac{1}{N} \sum_{i=1}^N P_2(\hat{t}_i \cdot \mathbf{n}) \right\rangle, \quad (1)$$

where P_2 is the second Legendre polynomial and \hat{t}_i is the vector tangent to the i -th repeat unit (Fig. 3b). To compute \mathbf{n} , we used the identity $S_2 = \mathbf{n} \cdot \mathbf{Q} \cdot \mathbf{n}$ ^{28,29}, where \mathbf{Q} is the tensor:

$$Q_{\alpha\beta} = \frac{1}{2N} \sum_{i=1}^N (3\hat{t}_{i\alpha}\hat{t}_{i\beta} - \delta_{\alpha\beta}), \quad (2)$$

δ the Kronecker delta, and $\alpha, \beta = x, y, z$; for a stable nematic phase, S_2 is the leading eigenvalue of \mathbf{Q} , and \mathbf{n} the corresponding eigenvector. We also computed the quantity $(S'_2)^2 = \langle P_2(\hat{t}(R) \cdot \hat{t}(0)) \rangle$ ²⁸, using as R the fibril's radius estimated from lateral density profiles (Figs. S7, S8¹⁸). S_2 and S'_2 are very similar in value (Fig. 3f), and the amide contact vector \hat{h} is nearly orthogonal to \mathbf{n} (Fig. 3g): both facts indicate a strong nematic phase²⁸.

A single director axis \mathbf{n} defines the predominant orientation among chains at both concentrations. This finding is in apparent contrast with measurements for long-chain PPTA ($n \sim 200$), showing an isotropic phase at concentrations as low as 2 wt%¹⁰. We attribute this difference to the combination of short chain length (up to $n = 18$, or $L_c = 230$ Å) and unit cell dimensions (up to 350 Å): both dimensions are comparable to the persistence length of PPTA in H_2SO_4 ($L_p \simeq 290$ Å by dynamic light scattering¹⁵). Confirming this estimate, we observe much wider undulations in the PPTA₁₈^z model (Fig. 2h, $L_c = 232$ Å) than in the PPTA₁₂ and PPTA₁₂^z models (Fig. 2b,e, $L_c = 155$ Å). Therefore, the conditions used lower significantly the critical concentration for the isotropic/nematic transition.

PPTA aggregates lack solid-crystalline order. Given the very high nematic order, we searched the simulated ensembles for the possibility of formation of solid nanocrystals. From the structure of the PPTA crystal⁴ we derived a metric ρ_{ij} to identify crystalline contacts between amide groups i and j using (i) the distance between the two groups' geometric centers $r_{ij} = |\mathbf{c}_j - \mathbf{c}_i|$, and (ii) the angle between two amide vectors, θ_{ij} :

$$\rho_{ij} = \frac{1}{2} \left(\frac{r_{ij}}{r_0} + \frac{\theta_{ij}}{\theta_0} \right) \quad (3)$$

where r_0 is equal to $r_0^{\parallel} = 6.6$ Å for i and j on the same chain and to $r_0^{\perp} = 5.3$ Å for i and j on different chains⁴, and $\theta_0 = 25^\circ$. We applied the DBSCAN method³⁰ to the metric ρ_{ij} with

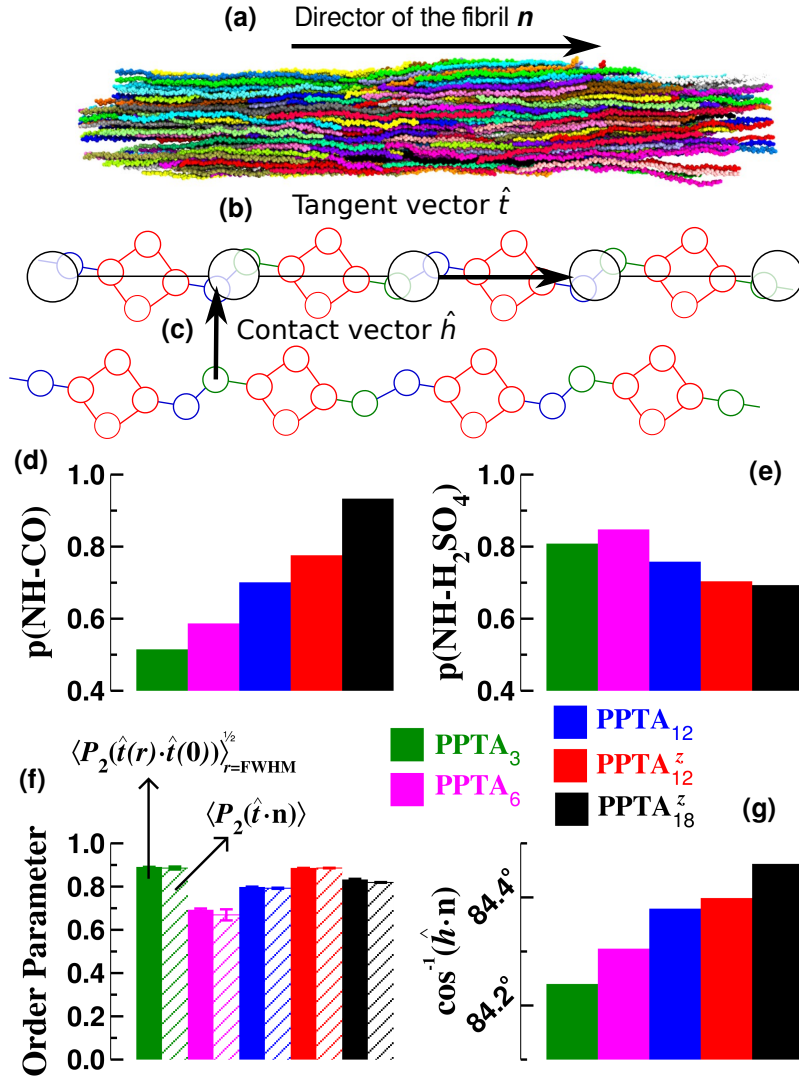


FIG. 3. PPTA chains in H₂SO₄ achieve a strong local nematic order, quantified using the following properties: the director \mathbf{n} , shown along the final snapshot of PPTA₁₂^z (a); the vector tangent to a PPTA chain's axis \hat{t} (b), the chain-chain contact vector, \hat{h} (c); probabilities of a NH...CO contact (d) and of a NH...H₂SO₄ contact (e); nematic order parameter calculated as in ref.²⁸ (f); mean angle between the vectors \hat{h} and \mathbf{n} (g).

a distance “cutoff” $\rho_0 = 1$ and a minimum cluster size of 7 (cubic lattice). As a control, this procedure correctly detects a single dominant cluster on a 5- μ s simulation of a pre-assembled crystal (Fig. 4c).

At each chain length considered, the computed cluster size distributions at 2 wt% and 20 wt% PPTA (Figs. 4a and S12¹⁸, respectively) are very similar to each other. This fact indicates that the characteristic structure of each chain is well sampled, and controlled solely by the chain length

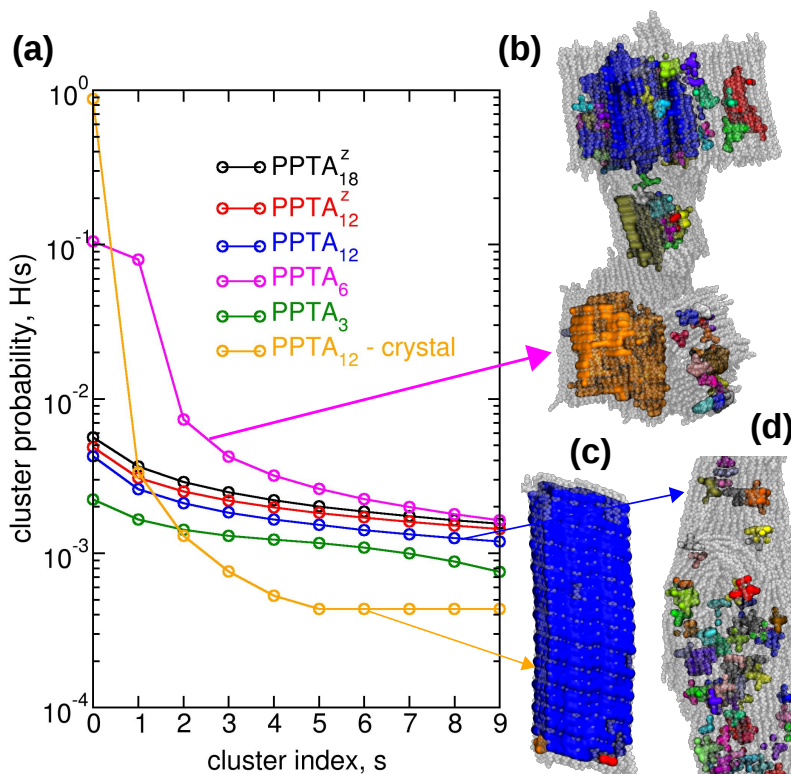


FIG. 4. Aggregates of PPTA chains lack solid-crystalline order. (a) Shown are the relative sizes of the 10 largest solid-crystalline clusters in simulations of 2 wt% PPTA in H_2SO_4x . Also shown are snapshots of $PPTA_6$ (b), a pre-assembled $PPTA_{12}$ crystal (c), and liquid-crystalline $PPTA_{12}$ (d); individual clusters are drawn in distinct colors for visualization purposes.

itself. $PPTA_6$ chains are the only ones to self-assemble in solid-crystalline clusters at both concentrations (Figs. 4b, S12¹⁸). Instead, PPTA chains with lengths $n = 3, 12$ and 18 remain in a liquid-crystalline form, and do not possess long-range solid-crystalline order: their clusters do not extend more than 2-3 polymer chains in the directions orthogonal to the chain axis. Even in the models where all chains share a single director axis ($PPTA_3$, $PPTA_{12}^z$ and $PPTA_{18}^z$), the strong orientational order does not appear to effectively promote crystallization.

H_2SO_4 insertions form long-lived point defects. While promoting a strong nematic phase, a possible unintended consequence of the use of H_2SO_4 is the formation of point insertion defects in PPTA fibers. Such defects (including H_2SO_4 molecules as well as $-SO_3H$ side groups) have been hypothesized to affect the mechanical properties of PPTA fibrils³¹. However, even relatively high concentrations only led to moderate (less than 20%) reductions in computed elastic moduli³¹. More importantly, the hypothesis that H_2SO_4 insertions remain embedded in the crystalline portion

of PPTA fibers (as opposed to the amorphous portion) has not been proven directly.

In the liquid-crystalline models here studied, we used the number of neighbors around each H_2SO_4 molecule as a classifier to identify H_2SO_4 molecules that appear kinetically trapped. Fig. 5 highlights such H_2SO_4 molecules, located near the central regions of the long-chain aggregates (PPTA_{12} , PPTA_{12}^z , and PPTA_{18}^z). Most of these molecules are arranged as evenly-spaced strands sheets with a nearest-neighbor distance of 4.1 Å (Fig. 5).

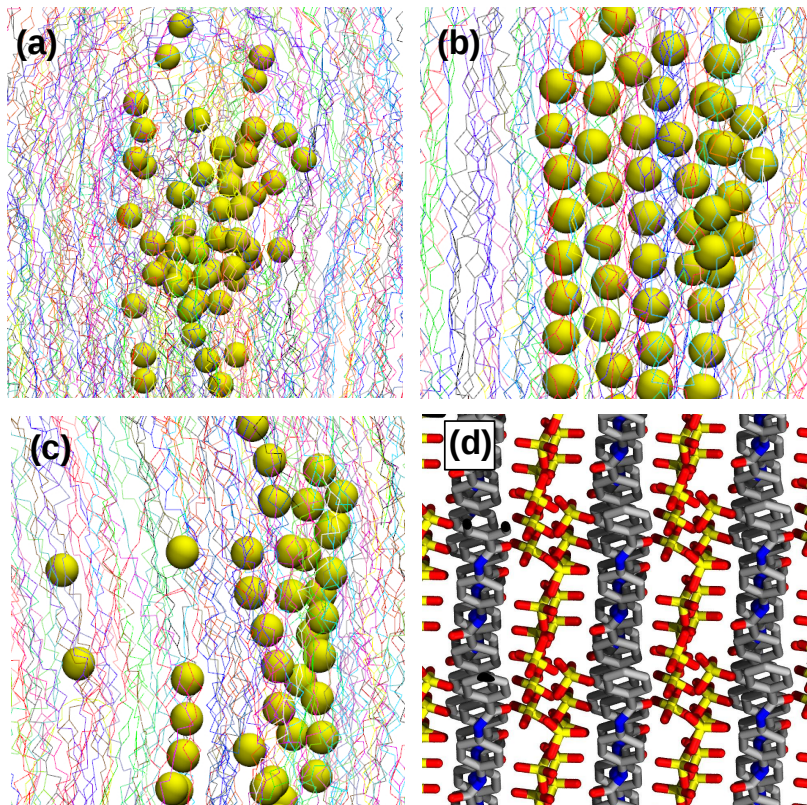


FIG. 5. Final simulation snapshots of (a) PPTA_{12} , (b) PPTA_{12}^z and (c) PPTA_{18}^z : buried H_2SO_4 molecules are shown as yellow spheres. (d) Crystallographic structure of p-phenylene-dibenzamide (PPDB) and H_2SO_4 ³²: the heavy atoms of a $3 \times 3 \times 3$ supercell are viewed from a direction parallel to the H_2SO_4 layers.

Layers of H_2SO_4 molecules were previously shown to be stable in an X-ray diffraction structure of the co-crystal of p-phenylene-dibenzamide (PPDB) and H_2SO_4 ³² (Fig. 5d). The spacing between amide groups along the (100) Miller vector of the PPDB- H_2SO_4 cocrystal is 9.75 Å³², which is very close to the 10.36 Å distance between the same groups along the (200) vector of the PPTA crystal⁴. Therefore, embedding a H_2SO_4 sheet in a PPTA crystal induces very little conformational strain on the crystal spacings.

In all simulations here described the amount of H_2SO_4 that remains trapped between PPTA chains is less than 0.1 wt% of the PPTA mass. It can be argued that much of that amount may be removed during fiber processing by pressure: however, single point defects can affect the mechanical strength of PPTA fibers, possibly by circumventing the steric clashes seen in the PPTA crystal⁴ and let the crystal yield when external forces are applied.

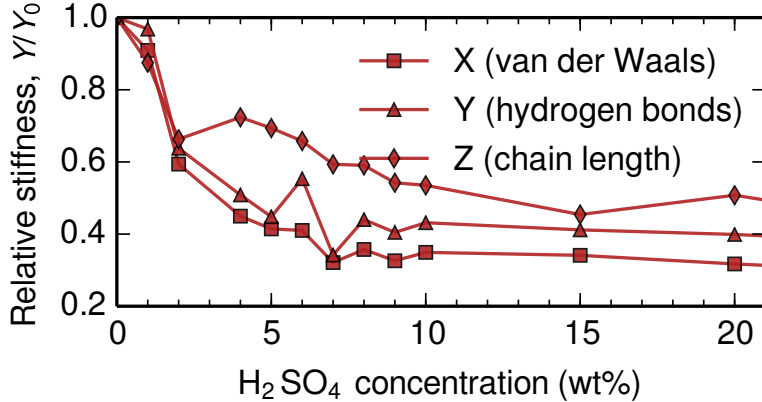


FIG. 6. Elastic properties of PPTA are affected by more than 1 wt% of H_2SO_4 . Each Young's modulus E is shown normalized with respect to its value computed on pristine PPTA.

Point defects weaken PPTA crystals. We computed mechanical properties of solid-crystalline PPTA to quantify the effect of H_2SO_4 on the performance of PPTA fibers. The changes in elastic moduli (tensile in the polymer chain/fiber direction, compressive in the orthogonal directions) are shown in Fig. 6. Each elastic modulus gradually decreases to about 50% of its pristine-PPTA value, and levels off after 4-5 wt% H_2SO_4 added to the PPTA crystal. Although such decrease in elastic constants could have macroscopic effects, commercial fibers do not contain such high amounts of H_2SO_4 . Conversely, we did not observe effects on elastic moduli at or below 1 wt% H_2SO_4 .

The above data indicate that a trace amount of H_2SO_4 do not have measurable effects on bulk elastic properties, largely because of the inability of the H_2SO_4 molecules to perturb the long-ranged order of PPTA chains, for the reasons discussed above. However, ballistic uses of PPTA fibers imply very high external forces, beyond the assumptions of small strain: the irrelevance of point defects can not be excluded under such conditions.

We tested the effect of trace amounts of H_2SO_4 (much smaller than 1 wt%) on the mechan-

ical response of PPTA crystals. To avoid introducing external biases, such as for example the co-localization of impurities and dislocations, we examined the effect of single point defects on an otherwise defect-free PPTA crystal, fully periodic in each direction (no chain ends). This configuration does not allow to simulate failure by tensile loads, for which finite-length chains must be used. Unfortunately, the use of chain lengths comparable to Kevlar[®] is also restricted by computational cost⁸. In the following, we use ideal crystals to test the resistance of PPTA against shear forces, the effects of which involve no dislocations along the chain length.

We simulated crystals of 100 and 400 PPTA₁₂ chains with and without a H₂SO₄ impurity, as well as crystals of 100 PPTA₁₂ chains with one and three interrupted bonds. The H₂SO₄ impurity is here represented by 10 H₂SO₄ molecules arranged in a linear strand parallel to the PPTA chains, similarly to the defects spontaneously formed (Fig. 5). This small strand corresponds to 0.3 wt% and 0.08 wt% H₂SO₄ in the 100- and 400-chain crystals, respectively. In the 100-chain crystal with three interrupted bonds (featuring a similar percentage of interrupted bonds as the commercial fibers), we set up the three chain ends at contiguous crystal sites.

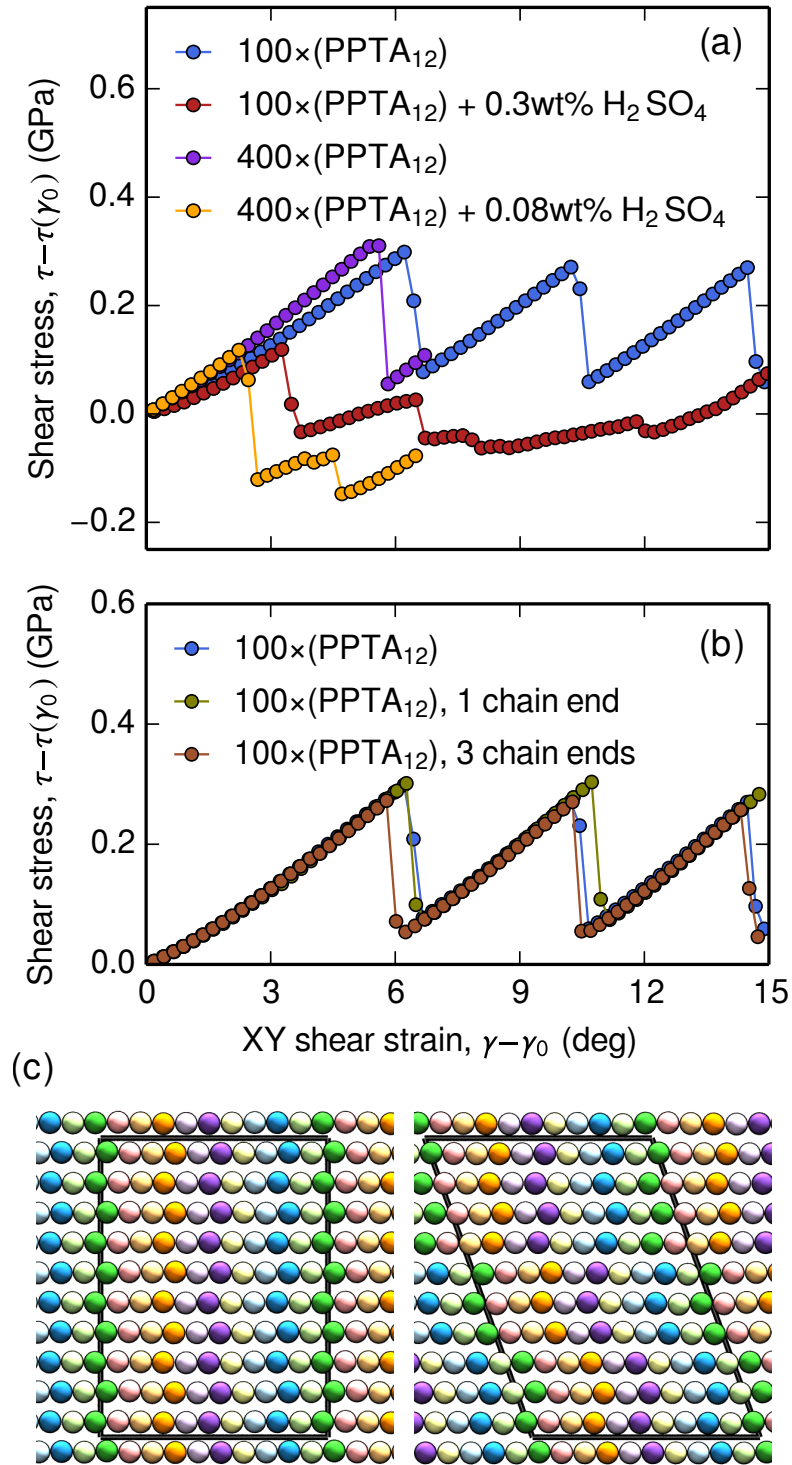


FIG. 7. Trace H₂SO₄ defects decrease the shear strength of PPTA crystals. Stress-strain curves are shown from the onset of the linear response ($\gamma \geq \gamma_0 = 8^\circ$) to the largest strain simulated. Pristine PPTA crystals are compared to crystals with a point H₂SO₄ defect (a) and with interrupted chains (b). Panel (c) illustrates the failure mode of PPTA crystals under shear: PPTA chains (spheres) are viewed along the fiber axis and colored based on initial position.

In all systems, small shear deformations ($\gamma < 8^\circ$) induce only a slow increase in stress τ (Fig. S13¹⁸), mainly dictated by the free-energy cost to mutually align the benzyl rings' planes: with the CG force field here used, such movements are enhanced compared to atomistic models^{8,33}. Beyond $\gamma_0 = 8^\circ$, τ increases linearly in all systems, reflecting the cost of chain-chain translations away from the energy minimum (Fig. 7). Predictably, none of the point defects affect the shear modulus G measured in this region, which depends only moderately on the model system's size: $G_{XY} = 2.7$ GPa and 3.1 GPa for the 100-chains and 400-chains crystals, respectively. This estimate compares well to the corresponding values from atomistic force fields, 3.9–6.1 GPa^{8,33}, and to the closely-related experimental measurement of the longitudinal shear modulus 2.9 GPa³⁴.

When subject to high shear strain, PPTA crystals with a point defect fail at a much lower stress τ_{\max} than pristine PPTA (Fig. 7a and Fig. S13¹⁸). Using as a common reference point the beginning of the linear regime, $\gamma = \gamma_0$, we observe that $\tau_{\max} - \tau(\gamma_0) = 0.30$ GPa for pristine PPTA and 0.11 GPa for PPTA with H₂SO₄ insertions, respectively. Remarkably, for each condition the 100- and 400-chain crystals give the same result, which appears to be independent on the model system's size.

In addition to featuring the highest yield strength, pristine PPTA crystals retain that strength over consecutive yield points (Fig. 7a). This is due to the failure mode by slippage, wherein the crystal recovers its original structure after each yield point (Fig. 7c). Crystals with interrupted chains also following this mode of failure (Fig. 7b), albeit at a moderately decreased strength ($\tau_{\max} - \tau(\gamma_0) = 0.26$ GPa). However, PPTA-H₂SO₄ systems fail by screw dislocations rather than by slippage, with the H₂SO₄ defect acting as a hinge (Fig. S14¹⁸): beyond the first yield strain, the periodicity of the crystal is compromised, and the shear stress τ never reaches τ_{\max} again.

We conclude that the effect of small impurities (less than 0.1 wt% H₂SO₄ in PPTA) goes largely undetected in the elastic regime, but can be catastrophic to the ultimate strength of crystalline PPTA fibers under the high-stress conditions of their intended applications.

IV. CONCLUSIONS

We used MD simulations to investigate the molecular structure of the PPTA-H₂SO₄ liquid-crystalline solution, observing the formation of local defects that impact the performance of solid PPTA fibers. Despite the relatively high number of particles in the simulated systems, the simulated PPTA chains are relatively short ($n \leq 18$, $L_c \leq 232$ Å) and do not extend beyond their

persistence length ($L_p \sim 290 \text{ \AA}^{15}$). Entanglement is absent in our models, and the diffusion of individual chains is impeded by chain-chain contacts but not prevented. Such contacts do not determine a preferred size for PPTA aggregates, and the results shown are stable with respect to the force field parameters. These facts indicate that the inhomogeneous liquid-crystal structure is very likely to also describe solutions of long-chain ($n > 100$) PPTA. Indeed, “blobs” of increased local alignment had previously been postulated, based on an analysis of bulk diamagnetic and dielectric anisotropies¹¹. Our observation is that both alignment and density are locally enhanced within these aggregates, which are prone to coalesce but are restrained from doing so by the conformational strain of PPTA chains in the absence of external forces. The inhomogeneity of the PPTA-H₂SO₄ solution can also facilitate the removal of bulk H₂SO₄ during the mechanical processing of the solution into solid fibers.

As a side effect of the coalescence between smaller fibrils, some H₂SO₄ molecules remain trapped between PPTA chains, becoming long-lived impurities. The total amount of H₂SO₄ trapped accounts for less than 0.1 wt% of the PPTA mass. We observed that such impurities, although uninfluential on the elastic properties of the enveloping crystals, are able to cause a dramatic loss of strength against shear deformations. This result indicates that the performance of materials such as Kevlar[®] or Twaron[®] under extreme conditions is controlled much more by their purity than by their crystallinity. In the design of new polyamide materials it may be more efficient to focus on solvent-free processes and less on improving crystallinity by itself.

ACKNOWLEDGMENTS

We are grateful to Axel Kohlmeyer, Kyle Hall, Jelena Matic and Jan Andzelm for fruitful discussions. This work was supported by the US Army Research Laboratory under contract number W911NF-16-2-0189. We also acknowledge partial support from the National Science Foundation instrumentation grant number 1625061.

¹ M. Panar, P. Avakian, R. C. Blume, K. H. Gardner, T. D. Gierke, and H. H. Yang, *J. Polym. Sci. B Polym. Phys.* **21**, 1955 (1983).

² M. G. Northolt, *Polym. Int.* **13**, 64 (1981).

³ Y. Rao, A. J. Waddon, and R. Farris, *Polymer* **42**, 5937 (2001).

- ⁴ M. G. Northolt and J. J. van Aartsen, *J. Polym. Science, Polym. Lett. Ed.* **11**, 333 (1973).
- ⁵ M. Plazanet, F. Fontaine-Vive, K. H. Gardner, V. T. Forsyth, A. Ivanov, A. J. Ramirez-Cuesta, and M. R. Johnson, *J. Am. Chem. Soc.* **127**, 6672 (2005).
- ⁶ R. J. Morgan, C. O. Pruneda, and W. J. Steele, *Journal of Polymer Science: Polymer Physics Edition* **21**, 1757 (1983).
- ⁷ M. G. Northolt, P. den Decker, S. J. Picken, J. J. M. Baltussen, and R. Schlatmann, “The tensile strength of polymer fibres,” in *Polymeric and Inorganic Fibers: -/-*, edited by . / (Springer Berlin Heidelberg, Berlin, Heidelberg, 2005) pp. 1–108.
- ⁸ B. Mercer, E. Zywicz, and P. Papadopoulos, *Polymer* **114**, 329 (2017).
- ⁹ M. R. Roenbeck, E. J. Sandoz-Rosado, J. Cline, V. Wu, P. Moy, M. Afshari, D. Reichert, S. R. Lustig, and K. E. Strawhecker, *Polymer* **128**, 200 (2017).
- ¹⁰ S. J. Picken, *Macromolecules* **22**, 1766 (1989).
- ¹¹ S. J. Picken, *Macromolecules* **23**, 464 (1990).
- ¹² S. J. Picken, S. Vanderzwaag, and M. G. Northolt, *Polymer* **33**, 2998 (1992).
- ¹³ A. M. Hindeleh and S. M. Abdo, *Polymer* **30**, 218 (1989).
- ¹⁴ E. I. du Pont de Nemours and Company, “Kevlar® aramid fiber technical guide,”.
- ¹⁵ Q. C. Ying and B. Chu, *Makromol Chem-Rapid* **5**, 785 (1984).
- ¹⁶ W. Shinoda, R. Devane, and M. L. Klein, *Mol. Simul.* **33**, 27 (2007).
- ¹⁷ R. DeVane, M. L. Klein, C.-c. Chiu, S. O. Nielsen, W. Shinoda, and P. B. Moore, *J. Phys. Chem. B* **114**, 6386 (2010).
- ¹⁸ See Supplemental Material at [URL will be inserted by APS] for additional computational details and supporting figures.
- ¹⁹ S. Mogurampelly and V. Ganesan, *Macromolecules* **48**, 2773 (2015).
- ²⁰ S. Nosé, *J. Chem. Phys.* **81**, 511 (1984).
- ²¹ H. C. Andersen, *J. Chem. Phys.* **72**, 2384 (1980).
- ²² M. Parrinello and A. Rahman, *J. Appl. Phys.* **52**, 7182 (1981).
- ²³ G. J. Martyna, D. J. Tobias, and M. L. Klein, *J. Chem. Phys.* **101**, 4177 (1994).
- ²⁴ D. Tanner, J. A. Fitzgerald, and B. R. Phillips, *Angew. Chem.-Int. Edit. Engl.* **28**, 649 (1989).
- ²⁵ W. Humphrey, A. Dalke, and K. Schulten, *Journal of Molecular Graphics* **14**, 33 (1996).
- ²⁶ W. Maier and A. Saupe, *Zeitschrift für Naturforschung A* **14**, 882 (1959).
- ²⁷ Y. Cao, Z. Liu, X. Gao, J. Yu, Z. Hu, and Z. Liang, *Int. J. Mol. Sci.* **11**, 1352 (2010).

- ²⁸ R. Eppenga and D. Frenkel, *Mol. Phys.* **52**, 1303 (1984).
- ²⁹ R. Pecheanu and N. M. Cann, *Phys. Rev. E* **81**, 041704 (2010).
- ³⁰ M. Ester, H. Peter Kriegel, J. Sander, and X. Xu, Proceedings of 2nd International Conference on Knowledge Discovery and Data Mining, 226 (1996).
- ³¹ M. Grujicic, P. S. Glomski, B. Pandurangan, W. C. Bell, C.-F. Yen, and B. A. Cheeseman, *Journal of Materials Science* **46**, 4787 (2011).
- ³² J. C. Calabrese and K. H. Gardner, *Acta Cryst. C* **41**, 389 (1985).
- ³³ D. J. Lacks and G. C. Rutledge, *Macromolecules* **27**, 7197 (1994), <https://doi.org/10.1021/ma00102a031>.
- ³⁴ S. Allen and E. Roche, *Polymer* **30**, 996 (1989).